Atmos. Chem. Phys., 8, 159–169, 2008
www.atmos-chem-phys.net/8/159/2008/

Atmospheric Chemistry and Physics

Scanning rotational Raman lidar at 355 nm for the measurement of tropospheric temperature fields

M. Radlach, A. Behrendt, and V. Wulfmeyer

University of Hohenheim, Institute of Physics and Meteorology, Garbenstrasse 30, 70599 Stuttgart, Germany

Received: 14 March 2007 – Published in Atmos. Chem. Phys. Discuss.: 31 May 2007
Revised: 16 November 2007 – Accepted: 12 December 2007 – Published: 15 January 2008

Abstract. For high-resolution measurements of temperature fields in the atmospheric boundary layer and the lower free troposphere a scanning eye-safe lidar which deploys the rotational Raman technique at 355 nm was developed. To optimize the filters of the receiver for both high nighttime and daytime performance, detailed simulation studies have been performed. The receiver is fiber-coupled to a sequential setup of multicavity interference filters used under small angles of incidence. Examples of nighttime and daytime measurements with the system which has a total power-aperture-efficiency product of 0.006 W m^2 are presented. Noontime temperature measurements with a temporal resolution of 60 s result in 1-sigma statistical temperature uncertainty of $<$1 K up to 1 km height and $<$2 K up to 2 km height. With an integration time of 60 min and a gliding average of 750 m a 1-sigma statistical temperature uncertainty of $<$1 K up to 14 km height is achieved during night.

1 Introduction

Temperature is a key parameter to describe the state of the atmosphere. It rules atmospheric stability. The observation of the diurnal variation of temperature layering in the free troposphere and the boundary layer is important for many meteorological processes e.g. the initiation of convection or the propagation of gravity waves. Thus for a comprehensive understanding of such processes, we developed an instrument which is capable of measuring temperature from close to the ground up to the tropopause with high accuracy and high temporal and spatial resolution. A scanner allows to perform these measurements in any direction of interest and hence to investigate spatial variability, especially, inside the atmospheric boundary layer and of the transition to the free troposphere.

The rotational Raman (RR) lidar technique for the measurement of atmospheric temperature was suggested by Cooney (1972). It makes use of the temperature dependence of the intensities of the rotational Raman lines. At date, the RR technique is the most reliable lidar method for temperature profiling (Behrendt, 2005) in the troposphere. Several ground based systems exist today (Vaughan et al., 1993; Nedeljkovic et al., 1993; Behrendt and Reichardt, 2000; Mattis at al., 2002) and even airborne (Behrendt et al., 2004a) and space-borne (Di Girolamo et al., 2006) application seems feasible.

Besides the RR technique also high spectral resolution lidar (HSRL) is used to measure tropospheric temperature profiles. The HSRL technique is resolving the temperature dependent linewidth of the Cabannes line which is Doppler broadened (Schwiesow and Lading, 1981; Shimizu et al., 1983). This technique poses much higher demands in respect to the stability of the system as shown in Hair et al. (2001) than RR lidar. Furthermore, it is difficult to achieve sufficiently high rejection of the Mie scattering (Hua et al., 2005a,b). While with the rotational Raman technique and state of the art interference filters, even measurements in optically thin clouds are possible (Behrendt and Reichardt, 2000).

So far, RR lidar systems have mainly been operated at the frequency-doubled wavelength of Nd:YAG lasers of 532 nm because of the higher laser power and receiver efficiency at this wavelength compared to the UV. Such systems are at date capable of temperature profiling up to the upper stratosphere (Behrendt et al., 2004b). In principle, UV wavelengths are advantageous to visible wavelengths because the rotational Raman backscatter coefficient is proportional to λ^{-4}. Attempts have also been made to use an UV wavelength for the lidar transmitter in the solar-blind region (Zeyn et al., 1996) but the first successful measurements in the UV to our

Correspondence to: M. Radlach
(radlach@uni-hohenheim.de)

Published by Copernicus Publications on behalf of the European Geosciences Union.

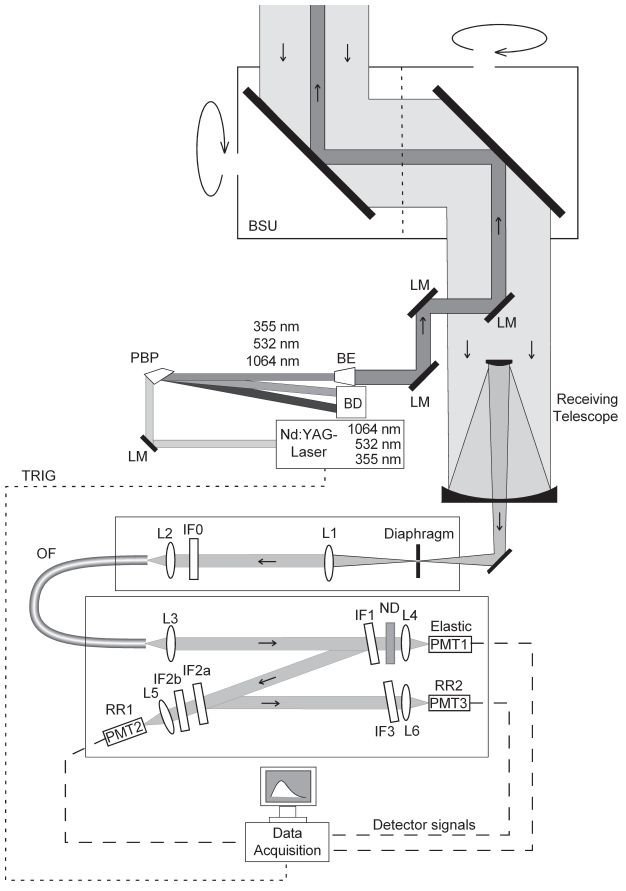

Fig. 1. Schematic setup of the scanning rotational Raman lidar system of UHOH. BD: beam dump, BE: beam expander, BSU: Scanner (beam steering unit), IF0–IF3: interference filter, L1–L6: lenses, LM: laser mirrors, ND: neutral density filter, OF: optical fiber, PBP: Pellin-Broca prism, PMT: photomultiplier tube, TRIG: trigger signal.

knowledge were made by Di Girolamo et al. (2004) with the frequency-tripled radiation of Nd:YAG laser of 355 nm. Daytime temperature profiling was demonstrated in the visible with gratings combined with a Fabry-Perot interferometer as a comb-filter (Arshinov et al., 2005) and with narrow-band interference filters (Behrendt et al., 2002; Di Girolamo et al., 2004). The better optical performance for narrow-band interference filters in the UV that can be realized today leads to a better system performance for tropospheric temperature profiling than for comparable systems in the visible domain because of the higher molecular backscatter coefficient and a higher efficiency of the detectors at lower wavelengths (Behrendt, 2005).

At University of Hohenheim (UHOH) we have developed a highly efficient RR lidar in the UV with a cascade filter mounting which is optimized for temperature measurements in the lower troposphere. This RR receiver setup was first introduced by Behrendt and Reichardt (2000) and was operated before only at 532 nm. In Sect. 2 the system setup of our scanning RR lidar is described. Section 3 gives a short overlook of the simulation of the filter parameters which we performed in order to select filter parameters optimized for our purposes. An example of a nighttime and a daytime as well as a scanning measurement is presented in Sects. 4–6. Conclusions are given in Sect. 7.

2 System setup

The scanning rotational Raman lidar of the University of Hohenheim (UHOH) is a mobile system which is mounted on a truck. The lidar setup is shown in Fig. 1. Technical specifications are listed in Table 1. As radiation source, a flash-lamp-pumped Nd:YAG laser (Spectra-Physics, model GCR5-30) with a output power of 9 W at the frequency-tripled wavelength of 355.66 nm and a pulse repetition rate of 30 Hz is used. In addition to the fundamental wavelength at 1064.0 nm, the laser emits radiation at 532.0 nm and 355 nm by frequency doubling and tripling simultaneously. The laser radiation at 355 nm is separated from the radiation at 1064 nm and 532 nm with a Pellin-Broca prism and is transmitted into the atmosphere after beam expansion to reduce both the energy density and the beam divergence. Care has to be taken to make the system eye-safe because of the capability of scanning operation of the lidar. The beam expansion ensures eye-safety beyond ranges of 400 m. The laser beam is emitted at the center of the receiving telescope (coaxial configuration). The roof-mounted scanner was manufactured by the workshop of the National Center for Atmospheric Research (NCAR) in Boulder, CO, USA, and is the same type as used in the Raman-shifted Eye-safe Aerosol Lidar (Spuler and Mayor, 2005) (REAL). The two scanner mirrors are pointing the beam in any direction of interest. The light backscattered from the atmosphere is directed via the same two scanner mirrors towards the telescope. The telescope is a Ritchey-Chretien type with a primary mirror diameter of 40 cm and an effective focal length of 4 m. After an adjustable field stop and a collimating lens the light passes the broadband interference filter IF0 with a transmission band of 8 nm full width at half maximum (FWHM). This filter blocks the atmospheric background light while the elastic and both rotational Raman signals are transmitted. An optical fiber guides the light into a polychromator box. The cascade structure of the polychromator (Behrendt and Reichardt, 2000) has some important advantages to other setups. First, the central wavelengths (CWLs) of the filters can be tuned by selecting the tilting angles. Second, we gain very high efficiency when separating the received light by a sequential mount of the channels. Finally, a very high suppression of at least 7 orders of magnitude of the elastically scattered light in the rotational Raman channels is achieved. Because the transmission band of IF2 is very close to the laser wavelength,

Table 1. Technical data.

Laser	
Type	Flash-lamp-pumped frequency tripled Nd:YAG laser, Spectra-Physics GCR5-30
Wavelength	354.66 nm
Pulse energy	≈300 mJ
Pulse repetition rate	30 Hz
Pulse duration	10 ns
Receiver	
Geometry	Ritchey-Chretien telescope
Primary mirror diameter	0.4 m
Telescope focal length	4 m
Field of view	0.75 mrad (selectable)
Polychromator	
Detectors	Hamamatsu R7400-U02 (elastic channel) Hamamatsu R1924P (rotational Raman channels)
Data acquisition system	3 channel Licel Transient recorder TR40-40 (analog and photon-counting) + opt-PR 2.5–20

we use two filters for the first rotational Raman channel. As shown in Table 2, already one order of suppression of the elastically scattered light is obtained at IF1 which reflects less than 10 % at the laser wavelength. The temperature is calculated with the ratio $Q(T)=P_{\mathrm{RR1}}(R,T)/P_{\mathrm{RR2}}(R,T)$ of the two RR signals $P_{\mathrm{RR1}}(T,R)$ and $P_{\mathrm{RR2}}(T,R)$ which depend on range R and temperature T.

An estimation results in a power-aperture-efficiency product of about 0.006 W m^2 for the full system including all optical components but the narrow-band interference filters IF1–IF3 which have peak transmissions of 0.62, 0.34 and 0.52 for the elastic, RR1 and RR2 channel, respectively. The values are mostly taken from manufacturers' data sheets but the reflectivities for the 3 consecutive laser mirros (LM) and both of the large scanner mirrors (Fig. 1) were measured by the authors.

The rotational Raman signals are extracted from the anti-Stokes branch like done before with other systems (Nedeljkovic et al., 1993; Behrendt and Reichardt, 2000; Behrendt et al., 2002; Di Girolamo et al., 2004). The transmission curves of the filters manufactured by Barr Associates, MA, USA, and the pure rotational Raman spectrum for N_2 and O_2 at temperatures of 250 K and 300 K are shown in Fig. 2. The filter parameters are listed in Table 2. They were selected according to the results of detailed optimizations described in Sect. 3.

The data acquisition is performed with a 3-channel transient recorder of Licel GmbH, Germany. The data of each channel are recorded as three signals: with 3.75 m resolution up to range of 15 km in analog and photon-counting mode and simultaneously in photon-counting mode with 37.5 m resolution up to a range of 76.8 km. This concept allows us to use the analog signals in the near range in which the photon-counting signals are saturated and the photon-counting signals in far range in which the signal-to-noise ratio of the analog data is low. It is then possible to combine the analog and the photon-counting data to get a single profile (e.g. Behrendt et al., 2004b; Whiteman et al., 2006; Pety et al., 2006).

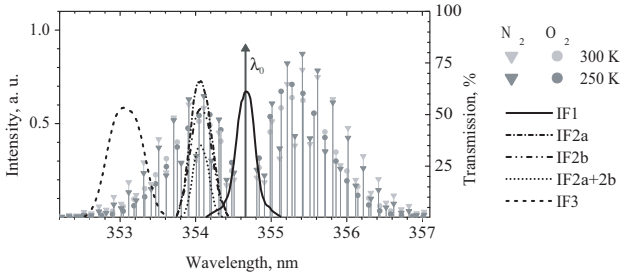

Fig. 2. Transmission curves of the narrow-band interference filters used in the rotational Raman lidar polychromator together with the rotational Raman spectrum of N_2 and O_2 for temperatures of T_1=300 K and T_2=250 K. λ_0 denotes the wavelength of the laser.

3 Filter optimization

For the investigation of most suitable filter parameters to extract the RR signals out of the backscattered light, we performed detailed simulations similar to those which have been described before (Nedeljkovic et al., 1993; Behrendt and Reichardt, 2000; Behrendt, 2005) but here with the focus on optimum performance in lower altitudes and in the presence of a daylight background signal. In these simulations, we calculated the statistical temperature uncertainty ΔT for different CWLs and filter width $\Delta\lambda_{\mathrm{FWHM}}$ (full width at half

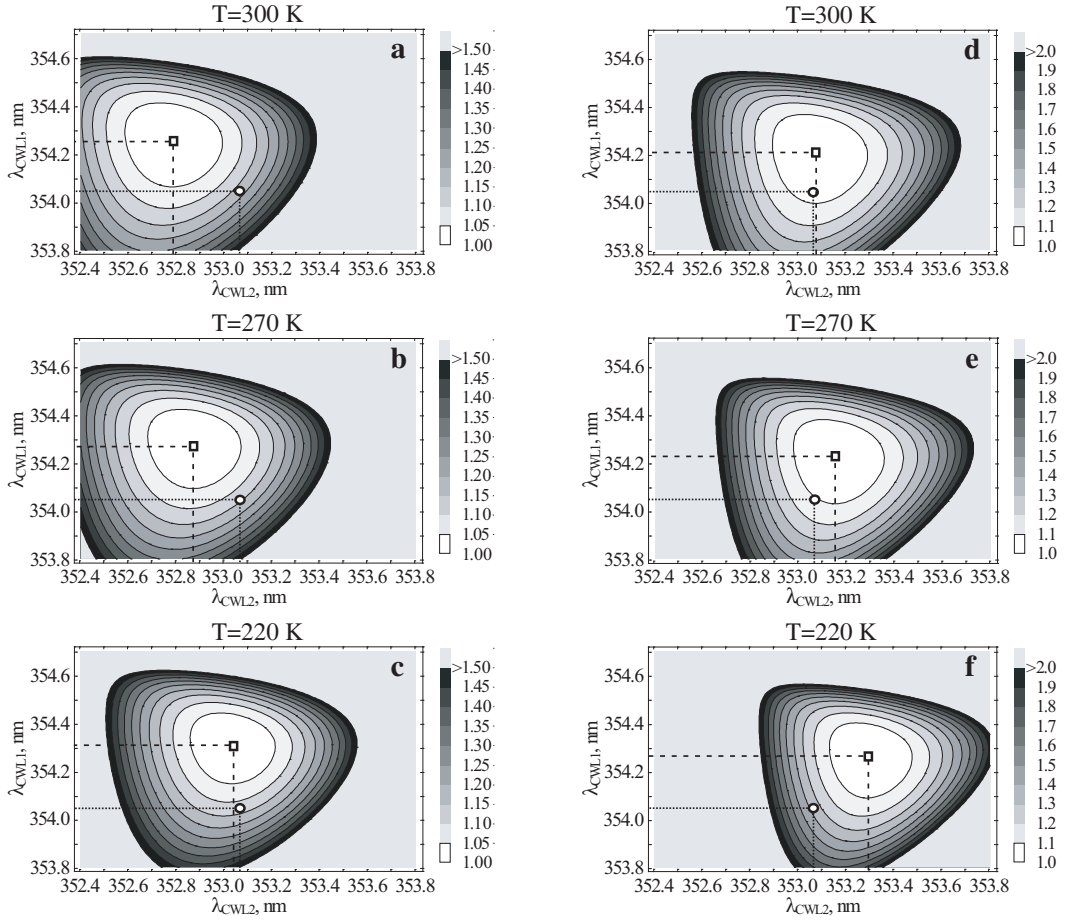

Fig. 3. Results of the optimization calculations for the parameters of the rotational Raman channel filters: Calculated statistical temperature uncertainty ΔT versus filter CWLs λ_{CWL1} and λ_{CWL2} for the filters shown in Fig. 2. Left: **(a)** (T_1, T_2)=(300 K, 305 K), **(b)** (T_1, T_2)=(270 K, 275 K) and **(c)** (T_1, T_2)=(220 K, 225 K). Right: same as (a–c) but with a background signal of the same intensity as the strongest rotational Raman line in the anti-Stokes branch added to the signals. Calculation step width was 0.01 nm. Values for ΔT are scaled relatively to the minimum (□) of each plot. The circle marks our setup. The gray scale of ΔT is plotted on the right.

maximum) at different atmospheric temperatures T. For the calculations we took into account the RR lines of N_2 and O_2. The 1-σ statistical temperature uncertainty can be calculated with

$$\Delta T = \frac{\partial T}{\partial Q}\Delta Q \approx \frac{(T_1 - T_2)}{(Q_1 - Q_2)} Q \sqrt{\frac{P_{RR1} + 2P_{B1}}{{P_{RR1}}^2} + \frac{P_{RR2} + 2P_{B2}}{{P_{RR2}}^2}}\,, \quad (1)$$

with P_{RR1} and P_{RR2} for the background corrected RR signals and Q the ratio of these two signals (Behrendt et al., 2004b). We calculated the uncertainties for different pairs of temperature (T_1, T_2) ranging from (220, 225 K) to (300, 305 K). Q_1 and Q_2 are the corresponding ratio values of the two extracted RR signals. P_{B1} and P_{B2} are the total background signals of each RR signal due to both detector noise and solar background. The statistical temperature uncertainties are minimum for a certain combination of high temperature sensitivity and large signal intensities dependent on temperature and background intensity.

We fulfilled different steps to attain our current filter specification. In the first step, we used a modified Gaussian curve to extract the signals out of the anti-Stokes branch in the simulations. The function is defined by

$$f(\lambda) = A \exp\left[-\left(\frac{2\,(\lambda - \lambda_{CWL})\,B}{\Delta\lambda_{FWHM}}\right)^4\right] \quad (2)$$

with λ_{CWL} the central wavelength at the peak transmission A and $\Delta\lambda_{FWHM}$ the filter width. B is describing the shape of the function and was chosen in a way that the resulting curve approximates the transmission curve of multicavity interference filters, in our case $B{=}\sqrt{\ln 2}$. The characteristics of this

Table 2. Filter parameters.

	IF0	IF1	IF2a	IF2b	IF3
AOI, deg	0.0	5.7	6.5	6.5	6.2
CWL, nm	353.65	354.66	354.05	354.05	353.05
FWHM, nm	8.5	0.29	0.32	0.33	0.52
Peak transmission	0.56	0.62	0.53	0.65	0.52
Reflectivity at 354.66 nm		<0.1			
Transmission at 354.66 nm	0.56	0.62	$<10^{-3}$	$<10^{-3}$	$<10^{-6}$

curve include very steep edges and an idealized transmission of 100% (A=1). To simulate daytime performance, we used a background signal per 0.1 nm of the spectrum which we scaled with a factor S relative to the intensity of the strongest RR line in the anti-Stokes branch. The background of each channel was then calculated for the respective filter width $\Delta\lambda_{\mathrm{FWHM}}$. We get therefore

$$P_B = S\frac{\lambda_{\mathrm{FWHM}}}{0.1\,nm}P_J^{\max} \quad (3)$$

with $P_J^{\max}$ as intensity of the strongest RR line in the anti-Stokes branch and $\Delta\lambda_{\mathrm{FWHM}}$ the filter width.

First calculations showed us that the most inappropriate filter bandwidth is at around 0.1 nm. For such narrow filters there is never more than one RR line of N_2 within the extracted signal because the RR lines are separated by >0.1 nm for a primary wavelength of 355 nm. The simulations showed that a pair of broader filters with different FWHM is the best choice. Below, $\Delta\lambda_{\mathrm{FWHM1}}$ is corresponding to the filter that extracts the RR signals close to the laser wavelength in the channel RR1 (in our case the pair of filters IF2a and IF2b) and $\Delta\lambda_{\mathrm{FWHM2}}$ corresponds to the filter which extracts the RR signals of higher rotational quantum states in the channel RR2 (IF3 in our case). When comparing equal transmission values $\Delta\lambda_{\mathrm{FWHM1}}=\Delta\lambda_{\mathrm{FWHM2}}=0.05$ nm with broader filters with $\Delta\lambda_{\mathrm{FWHM1}}=0.3$ nm and $\Delta\lambda_{\mathrm{FWHM2}}=0.5$ nm we found much lower statistical uncertainties in case of no background for the broader filters. This is due to the higher number of selected RR lines. But even with daylight background, ΔT for the broader pair of filters is almost equal to the pair with $\Delta\lambda_{\mathrm{FWHM1}}=\Delta\lambda_{\mathrm{FWHM2}}=0.05$ nm regardless of the intensity of the background. It is worth mentioning that transmission values for very narrow filters with FWHM=0.05 nm are feasible with around 15–20% at date. While filters with FWHM>0.3 nm can be manufactured with a transmission higher than 60%.

In the second step, we used realistic filter curves for our favored filter bandwidths of 0.3 nm for the first RR channel and 0.5 nm for the second RR channel. The filter curves were provided by Barr Associates, MA, USA, and included a realistic shape and transmission. In an iterative process, we optimized the CWL for low statistical measurement errors of RR temperature measurement under the condition to get at the same time sufficient suppression of at least 7 orders of magnitude of the elastically backscattered light in the RR channels. The optimum CWL we found for this configuration of filter pairs were ordered for an angle of incidence (AOI) of 5° to allow the sequential mounting and wavelength tuning.

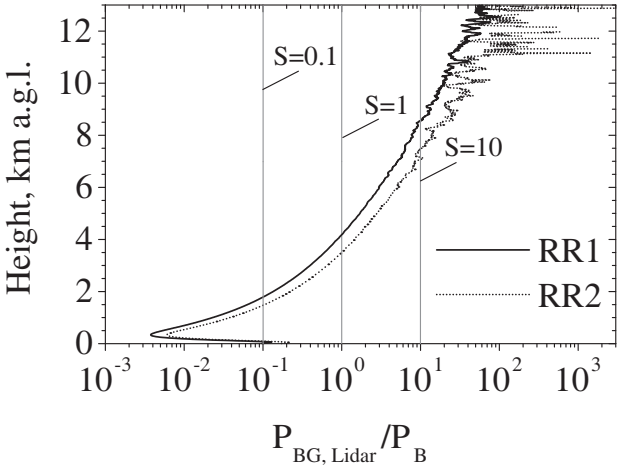

Fig. 4. Comparison of a measured daylight background in the RR channels RR1 and RR2 measured on 11 July 2006 at Hornisgrinde, 1161 m above sea level (a.s.l.) (Black Forest, Germany) between 11:30– 12:15 UTC to the simulated background P_B. Local noon is at 11:33 UTC. The ratio $P_{BG,\mathrm{Lidar}}/P_B$ is equal to the value of S which needs to be selected to obtain the measured background according to Eq. (3) for the simulation.

In the last step finally the optimum setup was simulated with the transmission curves of the manufactured filters (see Fig. 2 and Table 2) by calculating ΔT with Eq. (1). The calculations for atmospheric temperatures of (T_1, T_2)=(300 K, 305 K), (T_1, T_2)=(270 K, 275 K) and (T_1, T_2)=(250 K, 255 K) are shown without and with background signal in Fig. 3a–c and Fig. 3d–f, respectively. These simulations were performed for the wavelength of our laser of 354.66 nm. Figures 3a–c and Figs. 3d–f show that there is a pronounced shift of the optimum λ_{CWL2} towards longer wavelengths for decreasing temperatures, whereas there is

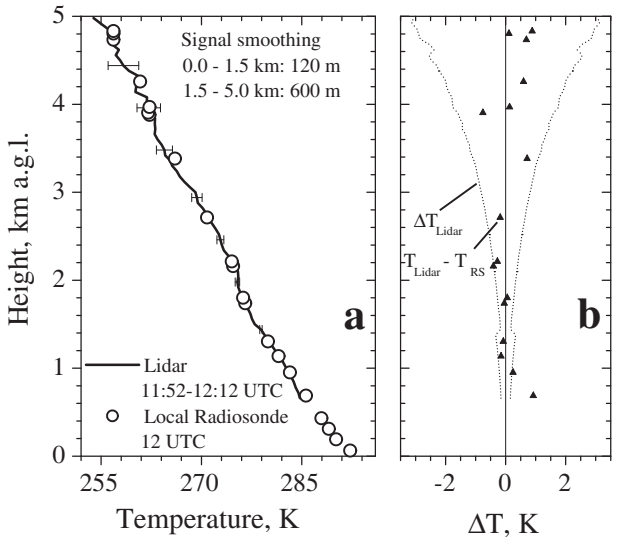

Fig. 5. Time-height cross section of 60-s temperature profiles between 11:52–12:12 UTC on 27 March 2006 at University of Hohenheim (Stuttgart, Germany) (left) and lidar profile with error bars (straight line) from 11:56 UTC and radiosonde (circles) from 12:00 UTC (right). Lidar signals were smoothed with a gliding average of 240 m. Error bars show the statistical temperature uncertainty.

only a very small shift for λ_{CWL1} for the temperature range investigated. In case of daytime performance in Fig. 3d–f with S=1 there is a shift towards longer wavelengths of λ_{CWL2} and a shift towards shorter wavelengths of λ_{CWL1} compared to the case without background (Fig. 3a–c). This shift also is barely increasing in case of $S \gg 1$. In conclusion, Fig. 3 show that we can fix λ_{CWL1} at one position and we afterwards can improve the system sensitivity by changing λ_{CWL2} by selecting the AOI depending on the background level present at the temperature range of interest. This can be done without any further adjustments of the other channels because the second RR channel is the last in the sequence. For the measurements presented in this paper, however, we decided to keep the filters fixed for optimum daytime performance and have not yet made use of this method for further improvements for nighttime measurements.

We had to offset λ_{CWL1} towards a shorter wavelength because of sufficient suppression of the elastic scattered light at the optimum position. For a temperature of 300 K this leads to an increase of statistical temperature uncertainties of just about 17% and 8% without and with daylight background, respectively. We obtain high performance in the lower troposphere like it is our goal. For other temperatures we got the following results: 270 K, uncertainties increase by 15% and 11% without and with daylight background, respectively; 220 K, uncertainties increase by 13% and 36% without and with daylight background, respectively.

To show that the artificial background signal used for the filter simulations is realistic, a typical measurement signal is compared with the simulations. The solar elevation angle was about 60° during the lidar measurement.

For comparison it is necessary to scale the theoretical derived background relatively to the measured background. This is done by $P_{Lidar}/P_{Simulation} \times P_B$. Figure 4 shows the ratio of the measured background signals $P_{BG,Lidar}$ to the theoretical P_B. It turns out that the simulations with the artificial background is matching the reality at about 4 km altitude. This height gives the point in which $P_{Lidar}/P_{BG,Lidar}$ is just equal to $P_{Simulation}/P_B$. Here the temperature was 267 K in this case. As P_{Lidar} is range-dependent and $P_{Simulation}$ is not a scaling factor of S=1 used for Fig. 3d–f is too high for heights below 4 km and too low above. It is important to note, that this does not affect our conclusions since no significant changes in optimum filter parameters were found for even much higher values of S. If S is matched to simulate the performance for higher temperatures (e.g. for heights at around 1.5 km S=0.1, which corresponds to a temperature of 285 K in that case) the optimum values for λ_{CWL2} is shifted towards shorter wavelength by 0.1 nm whereas λ_{CWL1} is not changed. In summary it can be stated that the performance simulations show that we can select filter parameters close to the optimum with and without daylight background and for a large range of temperatures.

4 Daytime measurements

The measurement example presented in this section is from 27 March 2006 at the site of University of Hohenheim, Stuttgart, Germany. The data were acquired at about noon between 11:52 and 12:12 UTC.

The lidar needs to be calibrated to obtain temperature. This is done by comparison of the ratio $Q(T)$ of the two RR signals with temperature profiles measured with radiosondes that are close in time and space to the lidar measurement. For the calibration we use $Q(T)=\exp(a/T+b)$ which is the exact function of $Q(T)$ for two isolated lines (Behrendt, 2005), T is temperature and a, b are calibration constants. We found in this case no differences worth considering the more complicated expression (Behrendt et al., 2002) $Q(T)=\exp(a'/T^2+b'/T+c')$.

The mean temperature profile measured during the 20-min interval is shown in Fig. 5 and a time-height cross section of 60-s temperature profiles in Fig. 6. The lidar data were acquired with a spatial resolution of 30 m and a temporal resolution of 60 s. For the calibration we chose a local radiosonde that was launched in a distance of 13 km to the lidar site. The analog signals were translated into virtual count rates by combining the analog and the photon-counting data (Behrendt et al., 2004b; Whiteman et al., 2006; Pety et al., 2006). The algorithm was applied in the height interval between 3 and 4 km. In Fig. 5a the lidar temperature profile together with the profile of a local radiosonde is shown.

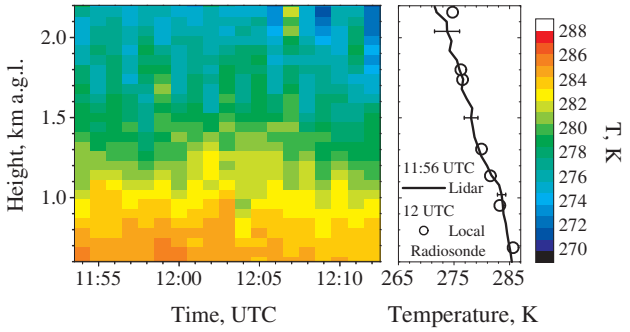

Fig. 6. **(a)** Lidar and radiosonde temperature profiles measured on 27 March 2006 at University of Hohenheim (Stuttgart, Germany). Lidar signals were smoothed with a gliding average of the indicated window lengths. Error bars are showing the statistical temperature uncertainty of the lidar profile. **(b)** Difference between lidar and radiosonde temperature and 1-σ temperature uncertainty of the lidar profile.

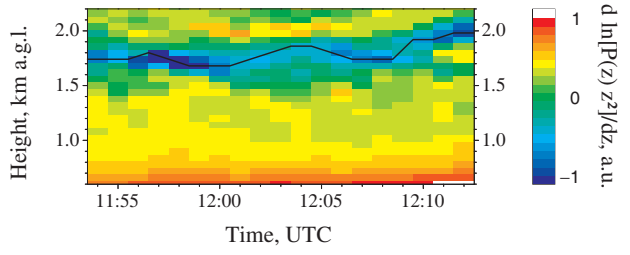

Fig. 7. Time-height cross section of the logarithm of the range corrected elastic signal on 27 March 2006 at University of Hohenheim (Stuttgart, Germany). The black line marks the boundary layer top.

Figure 5b shows the deviations between the lidar profile and the radiosonde as well as the statistical temperature uncertainty of the lidar profile. In this case the deviations are always smaller than 1-σ uncertainties of the lidar profile except at heights below 1 km above ground layer (a.g.l.) which are caused by natural differences in the boundary layer. The 1-σ statistical temperature uncertainties are not exceeding 3 K up to 5 km altitude a.g.l. and they are less than 1 K up to 3 km a.g.l. Figure 6 shows the time-height cross section of the 20-min time series. The profile of 11:56 UTC is shown on the right side. The statistical uncertainties are not exceeding 1 K up to 1 km a.g.l. and are well below 3 K up to 2 km height. The time-height cross section of the gradient of the logarithm of the range-corrected elastically scattered light as well as the temperature gradient is plotted in Figs. 7 and 8, respectively. From the data shown in Fig. 7 the boundary layer top was determined (black line). It can be seen that it is varying between 1.7 and 2.0 km a.g.l. during the measurement period. Normally the BL top is well defined by a temperature inversion or a lid. Such a lid is existing in the

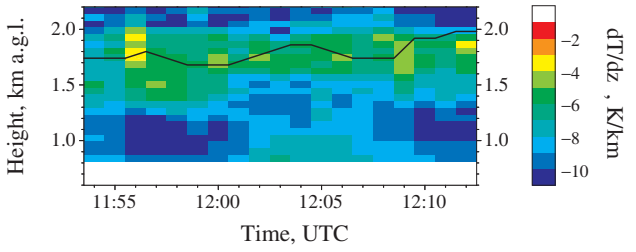

Fig. 8. Time-height cross section of the temperature gradient on 27 March 2006 at University of Hohenheim (Stuttgart, Germany). The black line is marking the boundary layer top derived by Fig. 7.

region of the BL top like seen in Fig. 8 with the temperature gradient. Values between −0.1 and 0.4 K/100 m mark the stable region which correlates with the BL top derived with the aerosol data.

5 Nighttime measurement: vertical

The measurement example shown in this and the following section were carried out during a campaign in the northern Black Forest in Germany. The campaign took place from 6–21 July 2006. The lidar site was situated on Hornisgrinde, the highest peak in the Northern Black Forest (8.2° E, 48.6° N) with an elevation of 1161 m above sea level (a.s.l.). During the campaign, radiosondes were launched in a distance of 3 km west of the lidar site at Brandmatt. This station was situated in a valley at an elevation of around 700 m a.s.l.

A nighttime measurement on 10 July 2006 is shown in Fig. 9. The signals were acquired between 20:00–21:00 UTC. Sunset was at 19:30 UTC. Figure 9a shows the temperature profile measured by RR lidar and the local radiosonde. This radiosonde was also used to calibrate the lidar. Because the sonde from Brandmatt reached only 14.7 km a.s.l. a radiosonde launched at 00:00 UTC from Munich is shown for larger altitudes. The radiosondes from Munich and Brandmatt were matching quite good in the upper free troposphere which shows the stable atmospheric conditions over southern Germany on that day. Figure 9b presents the statistical temperature uncertainty of the photon-counting signals and the deviations from the temperature profile derived by the lidar and that from the radiosondes. The statistical uncertainties of the lidar profile are below 1 K up to 13 km altitude a.g.l. which is just above the tropopause in this case. Beneath 600 m the lidar profile is distorted due to different overlap in the RR channels in the near field. In the future we plan to minimize these effects by the use of an aperture in front of IF2a in order to restrict the illumination of both PMT2 and PMT3 to the aperture of PMT3 (Behrendt, 2000). Furthermore, it is possible to use fiber scramblers for this purpose (Arshinov et al., 2004). The lidar profile is following the Munich sonde within the statistical

Table 3. Lidar temperature versus radiosonde at height intersections for the measurement example shown in Fig. 11.

Scan number	Range to radiosonde	Spatial distance of measurement points lidar–radiosonde	T_{RS}	T_{Lidar}	ΔT_{Lidar}	$T_{Lidar} - T_{RS}$
5	4.6 km	1.3 km	273.3 K	274.0 K	0.6 K	0.7 K
6	2.1 km	0.8 km	283.0 K	284.7 K	0.5 K	1.7 K
7	2.2 km	1.0 km	284.5 K	285.2 K	0.5 K	0.7 K
8	2.7 km	1.0 km	284.7 K	283.9 K	0.7 K	0.8 K
9	3.0 km	0.6 km	290.1 K	288.9 K	0.7 K	1.6 K

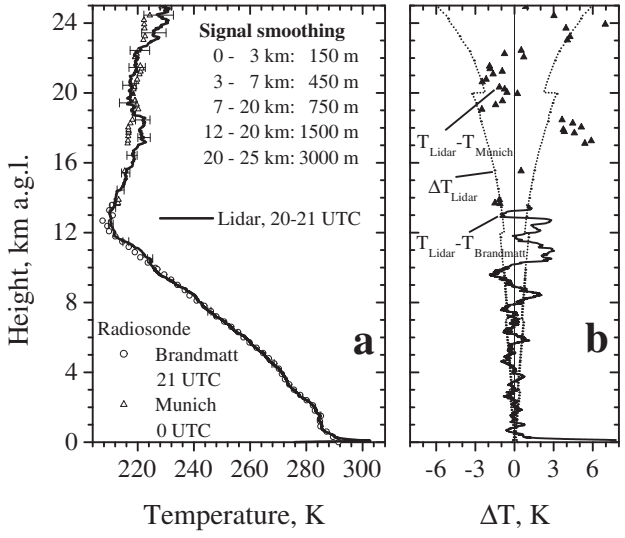

Fig. 9. (a) Lidar and radiosonde temperature profiles during night on 10 July 2006 on Hornisgrinde (Black Forest, Germany). Lidar signals were initially smoothed with a gliding average of the indicated window lengths. Error bars show the statistical temperature uncertainty of the photon-counting data. **(b)** Difference between lidar and the local radiosonde launched in Brandmatt and 1-σ temperature uncertainty.

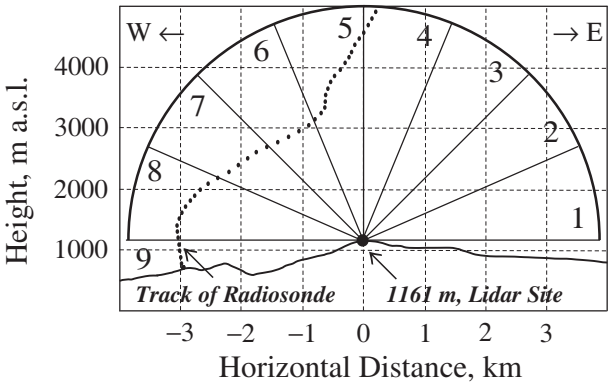

Fig. 10. Scan pattern and W-E cross section through the lidar site. Numbers from 1–9 are denoting directions in which profiles were measured. The track of the local radiosonde transposed to this plane, launched at 21:10 UTC, is illustrated by the dotted line.

temperature uncertainties above 14 km altitude. Larger differences of about 4 K between 16 and 19 km height might be caused by gravity wave activity above the lidar site.

The drift of the radiosonde during this ascent was mainly affected by a slow flow of 2–9 m/s. Up to 3 km a.s.l. the drift was basically towards the east. Beyond that level the sonde started circling around Hornisgrinde in a distance of 1–2 km by drifting to the southeast up to 5 km a.s.l. Above that level the ascent continued steadily northeastward. Up to a height of 9 km the sonde was within a circle of 3 km to the lidar site. It should be pointed out that the prominent feature of these deviations here is apparently wave-like (ΔT maxima in equidistant height of 2, 4, 6, 8 and 10 km) which coincides with the fact that the meteorological conditions were favorable for orographically induced gravity waves on that day.

6 Nighttime measurement: scanning

As first rotational Raman lidar, the system allows scanning measurements to investigate the variability of the temperature field. A scan pattern which we performed during a radiosonde launch is shown in Fig. 10. In the case presented here from 10 July 2006 we performed a zonal-RHI-scan (Range-Height-Indicator) with a constant step width of 22.5°. The lidar data was collected between 21:00 and 22:00 UTC. The temporal resolution for each pointing direction was 60 s. We performed 6 scans during the one-hour measurement period which were added up to improve the signal statistics. For the calculation of temperature profiles we used the calibration constants determined by the measurement in Sect. 5.

The track of the radiosonde is illustrated in Fig. 10 (dotted line). Starting from 21:10 UTC on the ground, it reached the upper end in the plot at 5 km altitude a.s.l. within 25 min. The sonde drifted primarily eastward up to a height of 3 km a.s.l. There was a pronounced wind shift from which on the ascent continued towards the southeast from 3 km altitude a.s.l. until the upper end of the image. The single temperature profiles

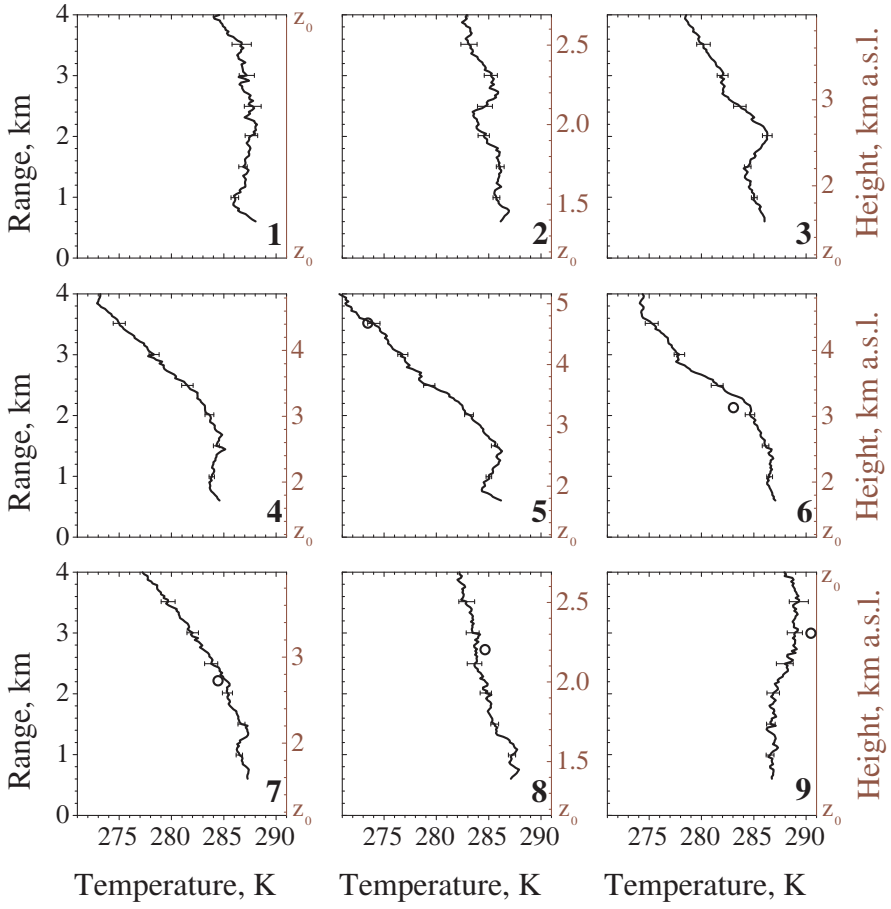

Fig. 11. Temperature profiles for each scan direction measured on 10 July 2006 from 21:00–22:00 UTC according to Fig. 10. The single profiles were averaged over 6 scans (=6 min) and a gliding average of 300 m until 1.5 km range, 600 m until 3 km range and 1200 m above 3 km range was applied. The black circles denotes the temperature measured by radiosonde at the corresponding height intersections. z_0 denotes the height of the lidar site of 1161 m a.s.l.

measured by the lidar are plotted in Fig. 11. Measurements where the radiosonde crossed the height level of the corresponding lidar profile are shown with a black circle. Table 3 summarizes these intersecting points. Lidar and radiosonde are in good agreement within the statistical uncertainties. At two points there are deviations larger than the uncertainties of the lidar data. The radiosonde station was located a little bit farther north to the lidar site and thus lidar profile 9 is sensing a volume about 600 m south of the radiosonde track, that easily leads to differences due to a different elevation of the orography. Close to the intersection with lidar profile 6 the radiosonde was entering a level with rapidly changing wind direction (from west to northwest) about 800 m down the valley respectively to the lidar. Wind shifts in the free troposphere very often are accompanied by temperature changes because of the advection of different air masses below and above the shift. The lidar profile 6 in Fig. 11 indicates the existence of such a layer that is potentially more elevated up the valley where the lidar measurement took place. The uncertainties of all profiles are less than 1.1 K in the plotted range of 4 km. Furthermore it should be noted that the lidar measurements present a temporal average while the radiosonde data provide a snapshot.

In contrast to radiosonde measurements and other remote sensing techniques, rotational Raman lidar can be used to analyze rather complicated meteorological conditions in complex terrain which can be seen in Fig. 12. Plotted are temperature gradients measured by lidar and radiosonde. The two lidar profiles are corresponding to the measurement shown in Fig. 9 and the vertical measurement of Fig. 11. All profiles show inversion layers below 3 km a.s.l. and several temperature lids above. The lidar profile measured between 20:00 and 21:00 UTC is matching the radiosonde quite closely, whereas the one of 21:00–22:00 UTC is pointing out changes in the shape of the inversion layer. This cannot be explained just by the different smoothing lengths which was doubled in the later measurement in the region where the inversion was observed. The complexness of the temperature field is

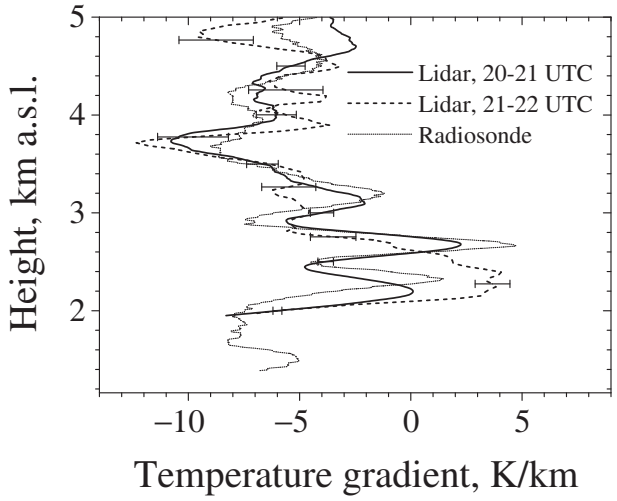

Fig. 12. Temperature gradients on 10 July 2006 of the lidar temperature profile measured between 20:00–21:00 UTC (Δt=60 min) (see Fig. 9), the lidar profile number 5 (Δt=6 min) from Fig. 11 and the radiosonde launched at 21:10 UTC.

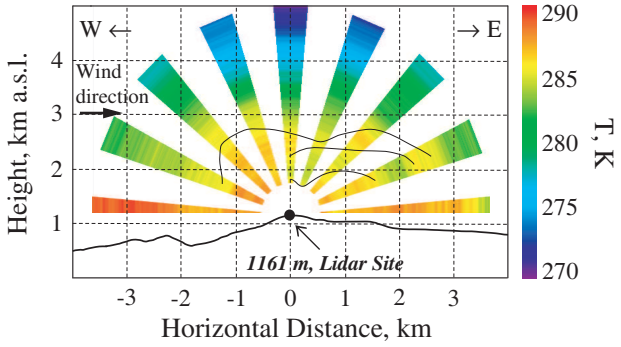

Fig. 13. Temperature field measured over Hornisgrinde on 10 July 2006 between 21:00–22:00 UTC (same profiles shown in Fig. 11). Lines mark the 285-K isotherm.

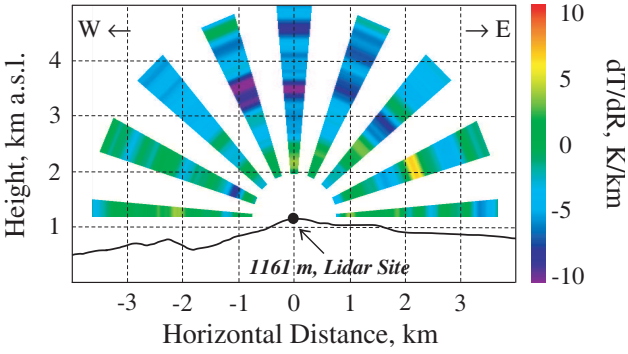

Fig. 14. Field of the temperature gradient along the line of sight calculated with the profiles shown in Fig. 11.

shown in Figs. 13 and 14 in greater detail. The temperature gradient in Fig. 14 corresponds to the gradient along the line of sight of the measurement. The air flowing against the mountain ridge is lifted up which causes a steep temperature gradient to the west (profile number 8 (see Fig. 10) at ranges around 1 km) in the direction of the measurement. Because of a stable atmosphere, the rising warm air is blocked at around 1.5 km a.g.l. just atop Hornisgrinde. To the east, a sequence of stable and more unstable regions developed. This can be seen in profile number 3 (see Fig. 10) in about 1 km and 2.2 km range as well as in profile number 2 in 2 km and 3 km range where the lowest temperature gradients are persisting bounded by stable layers. We believe that this shows gravity waves initiated at the mountain ridge.

7 Conclusions and outlook

We have developed a lidar for high-resolution rotational Raman temperature measurements at 355 nm. The receiver makes use of multicavity interference filters in a sequential setup. That way we gain very high efficiency when separating the signals and a high suppression of the elastically backscattered light in the rotational Raman channels. Furthermore, we are able to change the system's sensitivity by selecting the tilting angles of the filters. We performed simulations to optimize the filter parameters for RR temperature measurements for both high nighttime and daytime performance in the lower troposphere. A noontime temperature measurement resulted in uncertainties less than 1 K for ranges up to 1 km for 1 min integration time. The lidar allows to measure temperature fields by the use of a scanner. This gives a new tool to study, e.g. the highly complex structure of the temperature field over mountainous terrain. In the example shown, an averaging of the individual lidar profiles over 6 min and a spatial averaging, ranging from 300 m to 1200 m, yields in measurement uncertainties of smaller than 1.1 K up to a range of 4 km. Temperature profiling covering the whole troposphere up to 13 km altitude with statistical temperature uncertainties of less than 1 K is demonstrated with 60 min integration time.

It is noteworthy that the presented performance has still some room for improvement. To start with the temperature measurements at low range, we selected for the measurements presented here a receiver field-of-view of 0.75 mrad. A decrease of the field-of-view would significantly improve the daytime measurement performance but at the same time the range of partial overlap would be increased. By halving the field stop diameter the daylight background is already reduced to 25%. The performance can also be improved with better scanner mirrors. With newly coated mirrors, we expect a power-aperture-efficiency product of about 0.025 W m^2 instead of 0.006 W m^2 and thus an improvement of the resolution by a factor of 4. This will allow to measure temperature profiles in less than 1 min with a range resolution of better

than 300 m within the boundary layer without any extra daylight filter and an accuracy of $\Delta T < 1$ K.

Acknowledgements. This research was supported within the Convective Storms Virtual Institute (COSI-TRACKS) of the German Helmholtz Association. The authors are grateful to GKSS, Geesthacht, Germany to donate the mobile platform, to the Institute for Tropospheric Research, Leipzig, Germany, for the supply of the laser and to the National Center for Atmospheric Research, Boulder, CO for building the scanner and the technical support. Thanks to T. Schaberl for the interior fittings as well as to S. Pal for the support during the field campaigns.

Edited by: W. Ward

References

Arshinov, Y., Bobrovnikov, S., Serikov, I., Althausen, D., Ansmann, A., Mattis, I., Müller, D., and Wandinger, U.: Optic-fiber scramblers and fourier transform lens as a means to tackle the problem on the overlap factor of lidar, Proceedings of the 22nd International Laser Radar Conference, 227–230, 2004.

Arshinov, Y., Bobrovnikov, S., Serikov, I., Ansmann, A., Wandinger, U., Althausen, D., Mattis, I., and Müller, D.: Daytime operation of a pure rotational Raman lidar by use of a Fabry-Perot interferometer, Appl. Optics, 44, 3593–3603, 2005.

Behrendt, A. and Reichardt, J.: Atmospheric temperature profiling in the presence of clouds with a pure rotational Raman lidar by use of an interference-filter-based polychromator, Appl. Optics, 39, 1372–1378, 2000.

Behrendt, A.: Fernmessung atmosphrischer Temperaturprofile in Wolken mit Rotations-Raman-Lidar, doctoral dissertation (University of Hamburg, Hamburg, Germany), 2000.

Behrendt, A., Nakamura, T., Onishi, M., Baumgart, R., and Tsuda, T.: Combined Raman lidar for the measurement of atmospheric temperature, water vapor, particle extinction coefficient, and particle backscatter coefficient, Appl. Optics, 41, 7657–7666, 2002.

Behrendt, A., Nakamura, T., Tsuda, T., and Wulfmeyer, V.: Rotational Raman temperature lidar: New experimental results and performance expected for future ground-based and airborne systems, Proceedings of the 22nd International Laser Radar Conference, 2004a.

Behrendt, A., Nakamura, T., and Tsuda, T.: Combined temperature lidar for measurements in the troposphere, stratosphere, and mesosphere, Appl. Optics, 43, 2930–2939, 2004b.

Behrendt, A.: Temperature Measurements with Lidar, in: Lidar: Range-Resolved Optical Remote Sensing of the Atmosphere, edited by: Weitkamp, C., Springer, New York, 2005.

Cooney, J.: Measurement of atmospheric temperature profiles by Raman backscatter, Appl. Meteorol., 11, 108–112, 1972.

Di Girolamo, P., Marchese, R., Whiteman, D. N., and Demoz, B.: Rotational Raman Lidar measurements of atmospheric temperature in the UV, Geophys. Res. Lett., 31, L01106, doi:10.1029/2003GL018342, 2004.

Di Girolamo, P., Behrendt, A., and Wulfmeyer, V.: Spaceborne profiling of atmospheric temperature and particle extinction with pure rotational Raman lidar and of relative humidity in combination with differential absorption lidar: performance simulations, Appl. Optics, 45, 2474–2494, 2006.

Hair, J. W., Caldwell, L. M., Krueger, D. A., and She, C. Y.: High-spectral-resolution lidar with iodine-vapor filters: measurement of atmospheric-state and aerosol profiles, Appl. Optics, 40, 5280–5294, 2001.

Hua, D., Uchida, M., and Kobayashi, T.: Ultraviolet Rayleigh-Mie lidar with Mie-scattering correction by Fabry-Perot etalons for temperature profiling of the troposphere, Appl. Optics, 44, 1305–1314, 2005.

Hua, D., Uchida, M., and Kobayashi, T.: Ultraviolet Rayleigh-Mie lidar for daytime-temperature profiling of the troposphere, Appl. Optics, 44, 1315–1322, 2005.

Mattis, I., Ansmann, A., Althausen, D., Jaenisch, V., Wandinger, U., Müller, D., Arshinov, Y. F., Bobrovnikov, S. M., and Serikov, I. B.: Relativ-humidity profiling in the troposphere with a Raman lidar, Appl. Optics, 41, 6451–6462, 2002.

Nedeljkovic, D., Hauchecorne, A., and Chanin, M.-L.: Rotational Raman lidar to measure the atmospheric temperature from ground to 30 km, IEEE Trans. Geosci. Remote Sens., 31, 90–101, 1993.

Pety, D. and Turner, D.: Combined analog-to-digital and photon counting detection utilized for continous Raman lidar measurements, Proceedings of the 23rd International Laser Radar Conference, post deadline paper, 2006.

Shimizu, H., Lee, S. A., and She, C. Y.: High spectral resolution lidar system with atomic blocking filters for measuring atmospheric parameters, Appl. Optics, 22, 1373–1381, 1983.

Schwiesow, R. L. and Lading, L.: Temperature profiling by Rayleigh-scattering lidar, Appl. Optics, 20, 1972–1979, 1981.

Spuler, S. and Mayor, S.: Scanning Eye-Safe Elastic Backscatter Lidar at 1.54 μm, J. Atmos. Ocean. Technol., 22, 696–703, 2005.

Vaughan, G., Wareing, D. P., Pepler, S. J., Thomas, L., and Mitev, V. M.: Atmospheric temperature measurements made by rotational Raman scattering, Appl. Optics, 32, 2758–2764, 1993.

Whiteman, D. N., Demoz, B., Di Girolamo, P., Comer, J., Veselovskii, I., Evans, K., Wang, Z., Cadirola, M., Rush, K., Schwemmer, G., Gentry, B., Melfi, S. H., Mielke, B., Venable, D., and Van Hove, T.: Raman lidar measurements during the International H_2O Project. Part I: Instrumentation and Analysis Techniques, J. Atmos. Ocean. Tech., 23, 157–169, 2006.

Zeyn, J., Lahmann, W., and Weitkamp, C.: Remote daytime measurements of tropospheric temperature profiles with a rotational Raman lidar, Opt. Lett., 21, 1301–1303, 1996.